Review of Scientific Instruments

One-kilojoule pulsed-power generator for laboratory space sciences

Cite as: Rev. Sci. Instrum. **93**, 043505 (2022); https://doi.org/10.1063/5.0079450
Submitted: 21 November 2021 • Accepted: 01 March 2022 • Published Online: 08 April 2022

Po-Yu Chang (張博宇), **Yen-Cheng Lin** (林彥呈), **Ming-Hsiang Kuo** (郭名翔), **et al.**

AIP
Publishing

Rev. Sci. Instrum. **93**, 043505 (2022); https://doi.org/10.1063/5.0079450 **93**, 043505

One-kilojoule pulsed-power generator for laboratory space sciences

Cite as: Rev. Sci. Instrum. 93, 043505 (2022); doi: 10.1063/5.0079450
Submitted: 21 November 2021 • Accepted: 1 March 2022 •
Published Online: 8 April 2022

Po-Yu Chang (張博宇),[1,a] **Yen-Cheng Lin (林彥呈),**[1] **Ming-Hsiang Kuo (郭名翔),**[1] **Cheng-Han Du (杜承翰),**[1] **Chih-Jui Hsieh (謝知叡),**[1] **Mei-Feng Huang (黃梅鳳),**[1] **Ming-Cheng Jheng (鄭名城),**[1,2] **Jia-Kai Liu (劉嘉楷),**[1] **Sheng-Hua Yang (楊昇樺),**[1] **I-Lin Yeh (葉宜霖),**[1,3] **and Frank J. Wessel**[4]

AFFILIATIONS

[1] Institute of Space and Plasma Sciences, National Cheng Kung University, Tainan City 70101, Taiwan
[2] National Synchrotron Radiation Research Center (NSRRC), Hsinchu City 30076, Taiwan
[3] Department of Physics, UC San Diego, La Jolla, California 92093, USA
[4] L-Egant Solutions, LLC, 17165 Von Karman Ave., Suite 102, Irvine, California 92614, USA

[a] **Author to whom correspondence should be addressed:** pchang@mail.ncku.edu.tw

ABSTRACT

This paper reports on the assembly of a compact, low-cost, pulsed-power facility used for plasma studies. The construction uses two modules placed on opposite sides of the test chamber to minimize the system impedance and improve access to test samples. The stored energy is 1 kJ with a peak current of 135 kA and a 1592 ns quarter-period time. Up until now, an imploding conical-wire array has been studied by using time-integrated (visible) imaging, and time-resolved laser imaging, providing a measure of the plasma jet speed in the range of 170 km/s. Our future plans will continue to investigate high-energy-density plasmas that are relevant to the space environment, fusion, and spectroscopy.

I. INTRODUCTION

A broad variety of experimental techniques are used to simulate and measure the characteristics of plasmas for thermonuclear fusion, space physics, spectroscopy, etc. Prominent techniques include the use of pulsed-power electrical discharges produced by a variety of sources, including Marx generators, linear transformer drivers, and simple capacitor driven systems.

Conventionally used Marx generators are good experimental platforms to study the aforementioned scientific topics and include the Cornell Beam Research Accelerator (COBRA) at Cornell University;[1,2] the Mega Ampere Generator for Plasma Implosion Experiments (MAGPIE) at Imperial College London;[3] the Zebra generator at the Nevada Terawatt Facility, University of Nevada, Reno;[4] and the Z machine at Sandia National Laboratories.[5,6] The first three systems provide a peak current of ~1 MA with a rise time of 100–300 ns. The Z machine, on the other hand, provides a peak current up to 26 MA. These systems are typically quite large, requiring considerable effort and resources for their maintenance and operations, hence are not well-suited for a small, university-scale laboratory.

Recently developed linear transformer drivers (LTDs)[7–10] have become a popular alternative, e.g., the Michigan Accelerator for Inductive Z-pinch Experiments (MAIZE) at the University of Michigan,[11] Compact Experimental System for Z-pinch and Ablation Research (CESZAR) at the University of California San Diego,[12] and the High Amperage Driver for Extreme States (HADES) developed in the University of Rochester.[13] Such systems do not require the use of a pulse-forming line to produce a short-pulse (100–300 ns), high current discharge ($\gtrsim$100s kA). The size of a typical LTD is considerably smaller than conventional Marx, pulse-line-based systems.

Although the LTD seems to address the needs for a short pulse and high peak current, there remain challenges in building and operating the LTD. First, the system charging voltage is considerable (~ ±100 kV). Moreover, it uses many dozens of spark-gap switches that must be precisely synchronized. In addition, as the system inductance is very low ($\gtrsim$25 nH), the generator's output current may be heavily affected by the load inductance, especially loads that implode rapidly, reaching sizable final values.

Reported here is a design that employs the use of a double-sided, parallel-plate capacitive driver to attain a versatile, low-cost, and robust system that is simple to use and maintain in an academic-learning environment. The design is similar to the ZOT generator used previously at the University of California, Irvine.[14] In the ZOT generator, eight 6.25-μF capacitors in total were connected in parallel to increase the storing energy. The system was run at the charged voltage of 37.5 kV, giving a stored energy of 35 kJ. In our design, many submicrofarad range capacitors are connected in parallel. Although the structure is very similar to the ZOT generator, the main reason to connect many capacitors in parallel is to reduce the system inductance to the order of 100 nH, not just to increase the storing energy. In this way, we can use capacitors with higher internal inductance, which are cheaper and easier to obtain. Furthermore, only two discharge switches are used, which greatly reduces the need for precise synchronization as for an LTD. Finally, the system is charged to 20 kV with a stored energy of 1 kJ, unlike both the LTD and Marx generator systems.

Therefore, the direct-drive, parallel-plate, capacitor-driven system is much easier to build and operate, providing a pulse current of over hundreds of kiloamperes with a rise time in the order of 1 μs. The system reported here is named the Pulsed-power Generator for Space science (PGS) and is suitable for small loads, such as conical-wire arrays, exploding wires, and gas puffs. Up until now, we have used it to drive a conical-wire array and an x pinch. In the implosion of the conical-wire array, a plasma jet with a speed and corresponding Mach number comparable to the solar wind was produced.

The organization of this paper is as follows: In Sec. II, the description of the PGS machine is given. In Sec. III, the discharge test of the system is presented. In Sec. IV, we show the experimental results of driving conical-wire arrays and x pinches. Finally, a summary is given in Sec. V.

II. THE PULSED-POWER GENERATOR FOR SPACE SCIENCE (PGS)

Figure 1(a) is a computer-aided design (CAD) drawing of the PGS system, and Fig. 1(b) is a photograph of the assembled system. The dimensions for the assembled system are 4.3 m in length × 1.745 m in width × 0.83 m in height. The design provides easy access to the central-vacuum chamber, where the plasma loads are mounted. The trigger-pulse generator, the transformer, and the voltage doubler of the high-voltage power supply system (HV-PSS) are placed in the adjacent cabinet.

The two wings of the capacitor bank are connected in parallel, through parallel-plate transmission lines (PPTLs). The top plates of the PPTLs are connected to the outer cylinder of the cylindrical transmission line (CTL) and to the vacuum chamber, which is grounded to the earth ground. The bottom plates of the PPTLs are connected to the inner cylinder of the CTL. A load depending on different experiments is connected between the outer and the inner cylinders to close the current path. The inner cylinder of the CTL is connected to the earth ground through a 5 MΩ resistor, which is part of the circuit used to charge the system. Details of each component are described in the following.

The circuit schematic for the system is displayed in Fig. 2. The capacitor bank is divided into two parts (north and south “wings”), each switched by a rail-gap, with their pulses delivered by a parallel-plate transmission line interfaced to a common coaxial-transmission line that is located in a central vacuum chamber. The diagnostics include a Rogowski coil for the current measurements; a time-integrated, visible-imaging system; a time-resolved shadowgraph imaging system; and a time-resolved schlieren imaging system. Shadowgraphy and schlieren imaging use a Q-switched Nd:YAG laser with a temporal resolution in the order of nanoseconds.

A. Capacitor bank

Twenty 1 μF capacitors comprise the energy-storage bank. The system is charged to 20 kV storing 1 kJ of energy. Two 1-kΩ resistors connected in series with two high-voltage diodes protect the HV-PSS in case a prefire occurs during the charging phase. For the same reason, the 10-MΩ resistor is connected to the trigger-pulse generator. The HV-PSS is connected to all capacitors through normally open (N.O.) relays. To protect the HV-PSS, N.O. relays are opened just before rail-gap switches are triggered so that the HV-PSS is disconnected from the pulsed-power system. The 2- and 1-GΩ resistors set the potentials of the rail-gap triggering electrodes equal to one-third of the charging voltage. Two 40-pF capacitors maintain the voltage difference between the trigger-pulse generator and the triggering electrodes during the charging phase. The negative high-voltage trigger pulse, with a fast rise time, propagates through the

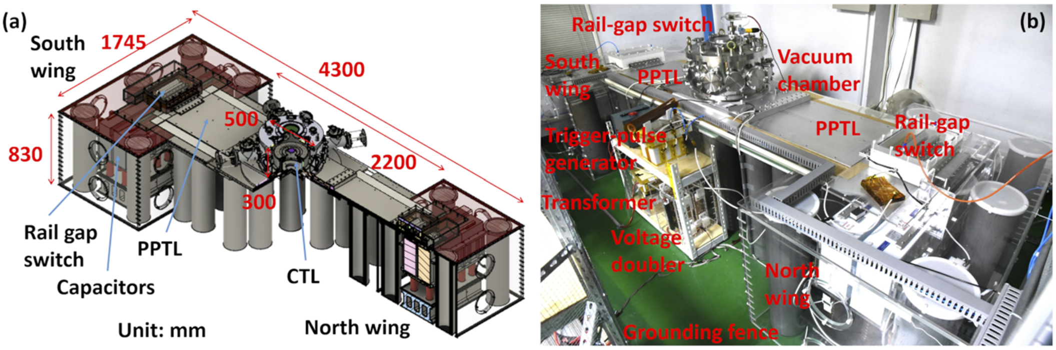

FIG. 1. (a) CAD drawing for the PGS machine with a cut view of the chamber and the north wing. (b) Photograph of the PGS machine, without diagnostics.

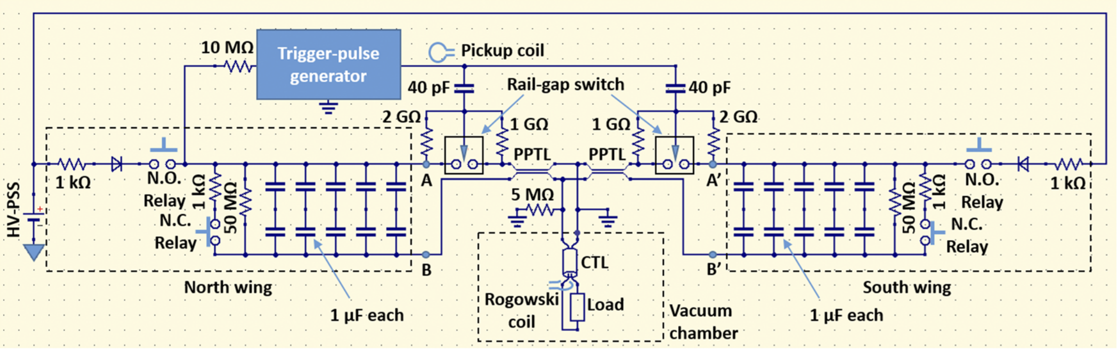

FIG. 2. Circuit schematic of the PGS system.

capacitors, activating the rail-gaps. In contrast, the capacitors block the relatively slow main pulse so that the trigger-pulse generator is not damaged.

Capacitors in each wing are mounted 425.5 mm above the floor (for safety) and enclosed in an acrylic box so that dust particles do not get into the capacitor bank. The acrylic box also serves as a dielectric barrier. The average annual humidity in Taiwan is close to 80%; no special precautions are used to prevent HV arcing.

The energy in each wing can be dumped in ~20 ms when the relay is closed. Two bleeder resistors are connected to the capacitors in each wing: a 1-kΩ, 1.5-kW high-power wire-wound resistor that is connected to capacitors through a normally closed (N.C.) pneumatic high-voltage relay, and a second 50 − MΩ resistor that safely discharges the entire energy within ~16 min whenever HV-PSS is disconnected from the energy bank.

B. Rail-gap switches and the trigger-pulse generator

Custom-built rail-gap switches were developed for the system.[15–20] The inductance of the rail-gap switches is ~80 nH.[20] The 304 SS rail-gap electrodes have a diameter of 50 mm and a length of 300 mm. The distance between the electrodes is 11 mm and the triggering electrode is mounted 4 mm away from the electrode that is connected to the PPTL.

The self-breakdown voltage for the rail-gaps exceeds 29 kV. To trigger the rail-gap switches and generate multichannel discharge in the switches, a high-voltage triggering system provides a negative high-voltage trigger pulse lower than −40 kV with a falling speed of −6.6 ± 0.4 kV/ns. More details of the rail-gap switches and the trigger-pulse generator were given in Ref. 20.

Dry air is used to purge all discharge switches, including those used in the three-stage trigger Marx; the flow-rate is 8 l/min.

C. Parallel-plate transmission lines

Parallel-plate transmission lines (PPTLs) transfer the current from each wing of the capacitor bank to the bottom of the cylindrical vacuum chamber, where the high-voltage feedthrough is located as shown in Figs. 1 and 3. For each PPTL, two aluminum plates with a thickness of 10 mm and a width of 600 mm are used. Twenty Mylar sheets (thickness 0.188 mm, total thickness of 3.76 mm) are used to insulate the two metal plates of the PPTL. The width of the Mylar sheets is 1000 mm, i.e., Mylar sheets are extended 200 mm over the metal plates on each side to prevent flashover across the side of the insulation layer.

During the main discharge, the current from each wing of the capacitor bank flows along the top plate of the transmission lines to the high-voltage feedthrough. The return current flows through the bottom plate of the transmission lines back to each wing of the capacitor bank.

D. High-voltage feedthrough

The high-voltage feedthrough at the bottom of the vacuum chamber is shown in Fig. 3, and the enlarged drawing is shown in Fig. 4. It is used to convert the current flow from horizontal to vertical, combining the currents from each wing of the capacitor bank, and delivering it to the target through the CTL. The feedthrough is formed by three plates stacking on top of each other. An insulation disk is sandwiched between two rectangular metal plates. The top metal plate is also the bottom plate of the vacuum chamber. It is an aluminum plate with a thickness of 25 mm, a width of 600 mm, and a length of 1000 mm. The vacuum chamber introduced in Sec. II E sits at the center of the top metal plate. The top metal plate is attached to the top plates of both PPTLs. At the center of the top metal plate,

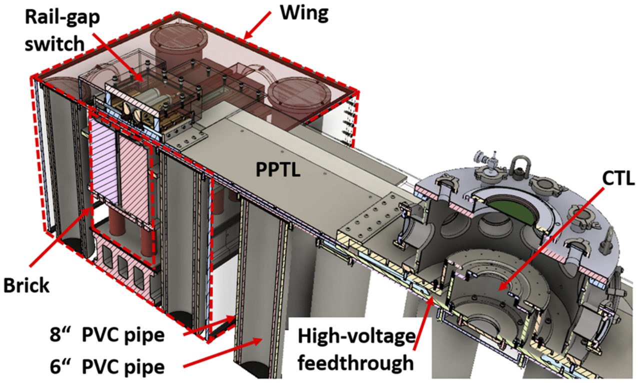

FIG. 3. Cut-away CAD drawing of the PGS system.

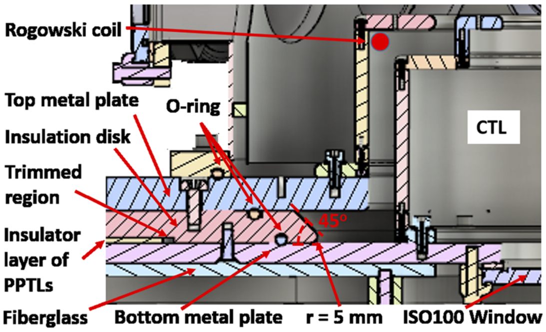

FIG. 4. Detailed CAD drawing for the high-voltage feedthrough.

there is a circular hole with a diameter of 300 mm. The hole is for adapting the CTL introduced in Sec. II F. On the other hand, the bottom metal plate is an aluminum plate with a thickness of 15 mm, a width of 600 mm, and a length of 1100 mm. It is attached to the bottom plates of both PPTLs. It is also attached to the inner cylinder of the CTL. There is a circular hole at the center of the bottom metal plate covered by an ISO100 window. It can be used for diagnostics from the bottom if necessary. Finally, a polyethylene (PE) disk with a diameter of 1000 mm and a thickness of 24 mm is used as the insulation disk. At the center of the PE disk, there is a circular hole with a diameter of ~360 mm. As shown in Fig. 4, the sidewall of the hole is tilted 45° and rounded with a radius of 5 mm to prevent flashover through the sidewall. Furthermore, the bottom side of the PE disk is trimmed down 4 mm. The inner radius of the trimmed region is 600 mm. The insulating layer of the PPTL is inserted into the trimmed region to prevent the flashover through the connection between PPTL and the high-voltage feedthrough. When the system is activated, currents from both wings of the capacitor bank will flow through the top plate and to the outer cylinder of the CTL. After the current flows through the load attached to the CTL, the return current from the inner cylinder will flow through the bottom plate and back to both wings of the capacitor bank through the bottom plates of both PPTLs.

E. Vacuum chamber

Experiments are conducted in high-vacuum in the cylindrical-central chamber, mounted on top of the high-voltage feedthrough. The stainless steel chamber dimensions are 500 mm diameter × 300 mm long, as shown in Fig. 3.

Twelve ISO100 flanges are circumferentially welded to the mid-plane of the vacuum chamber 150 mm above the bottom and are used for inserting diagnostics. A turbomolecular pump (220 l/s) is connected to one of the ISO100 flanges on the side. A dielectric break is inserted between the pump and the chamber to prevent damage to the pump when the main discharge is fired. An uninterruptible power supply (UPS) system is used as additional protection, which is disconnected from the power mains just before each shot. The chamber is pumped down to the order of 10^{-6} Torr for experiments.

An ISO200 flange is welded at the center of the top lid. An additional eight KF40 flanges are used for electrical feedthrough for diagnostics, pressure gauges, and the venting valve.

F. Coaxial-transmission line

As shown in Fig. 3, a set of a coaxial-transmission line (CTL) made of stainless steel at the center of the vacuum chamber orientates vertically is used. It is attached to the high-voltage feedthrough, which is also the bottom plate of the vacuum chamber. The outer diameter of the inner cylinder and the inner diameter of the outer cylinder are 260 and 300 mm, respectively. An adapter for connecting different targets is connected to the top end of the CTL. The inner disk of the adapter is the cathode, while the outer disk of the adapter is the anode. The outer diameter of the inner disk and the inner diameter of the outer disk are 200 and 170 mm, respectively. The total length of the CTL is 120 mm, i.e., ~30 mm below the middle plane of the chamber. Therefore, when targets with the finite height for experiments are installed at the center of the vacuum chamber, all ISO100 flanges can be used to observe experiments.

G. Diagnostics

There are several diagnostics used on the PGS machine: a Rogowski coil for current measurement, a time-integrated imaging system in the visible light region, and a time-resolved imaging system using an Nd:YAG Q-switch laser backlighter. The time-resolved imaging system includes shadowgraphy and schlieren imaging.

1. Rogowski coil

A Rogowski current monitor is used to measure the discharge current and is located between the CTL, as indicated by the red dot in Fig. 4. The coil is made by using an RG58 coaxial cable, as shown in Fig. 5. The length of the cable is ~872 mm. One end of the cable is connected to a BNC connector. The outer insulation layer and the

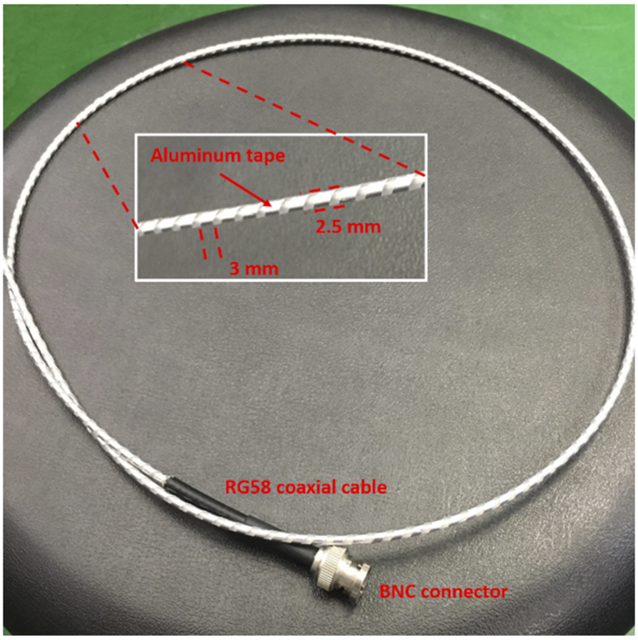

FIG. 5. Rogowski coil constructed using aluminum tape to make the helical coil.

outer conducting layer were ripped off. An aluminum tape with a width of 3 mm was then wrapped around the coaxial cable as the helical coil of the Rogowski coil, as shown in the inset of Fig. 5. The number of turns of the helical coil is 130. The diameter of the helical coil is 2.5 mm. One end of the helical coil is attached to the center conductor of the coaxial cable and the other end is attached to the ground of the BNC connector. For insulation, the Rogowski coil is placed inside a polyurethane (PU) tube with the inner and outer diameters of 4 and 6 mm, respectively. Finally, another RG58 coaxial cable is connected between the BNC connector of the Rogowski coil and a BNC feedthrough on one of the KF40 flanges on the lid of the vacuum chamber. Then, an R–C integrator is used to integrate the signal. The resistance and the capacitance of the integrator are 5 kΩ and 48 nF, respectively. Therefore, the voltage output from the integrator directly provides the total current of the PGS machine. The convertion ratio between the discharge current and the voltage output of the integrator is 188.0 ± 0.3 kA/V.

2. Time-integrated imaging system

The system captured images from one of the ISO100 windows in the direction indicated in Fig. 6. The system is a Raspberry Pi HQ camera that uses a Sony IMX477R CMOS image sensor. The camera is powered by batteries, controlled wirelessly, and enclosed in an aluminum box. Therefore, it is resistant to the electromagnetic pulse (EMP) noise from the discharge of the PGS machine. The focal length of the lens is 50 mm for the imager size of 1/1.2 in. The f-number is $f/16$, and the ISO sensitivity is ISO1. However, the self-emission is still too bright, so a neutral-density (ND) filter with an optical density of 64 is used. Note that the discharge current drains in the order of microseconds, which is much shorter than the opening time of the fastest shutter. Thus, the exposure time depends on the plasma's self-emission time, not on the time that the shutter remains open. Therefore, the shutter is kept open for 15 s. We only need to ensure that no light is leaked into the chamber and the PGS machine is triggered within 15 s. In this case, the time-integrated self-emission of the plasma will be captured by the camera.

3. Time-resolved imaging system

To capture time-resolved images, an Nd:YAG Q-switch laser, Q-smart 850-2w SLM made by Lumibird,[21] is used. The laser generates a burst of laser light with a pulse width of ~5 ns in 532 nm. The timing jitter of the laser is 1 ns. Figure 6 shows the design of the optical beam path of the laser diagnostics. The half-wave plate (HWP) and the polarizing beam-splitter cube (PBS) on "Optical table 1" are used to control the laser energy that is delivered to the vacuum chamber. Although the energy of the laser burst is up to 290 mJ per pulse, only 15.2 ± 2.0 mJ per pulse is delivered to the target. On the other hand, the portion of the laser beam passing through the PBS is blocked by a beam dump (BD). The scattered light from the beam dump is captured by a photodiode (PD), a biased Si detector DET10A2 made by Thorlabs.[22] Therefore, we measure the timing of the laser light relative to the current output *in situ*. The laser beam is expanded to size with a diameter of ~30 mm, which is the field of view, by the lenses "f-50" and "f200." Cameras for taking shadowgraph and schlieren images are the same as that used in the time-integrated imaging system. They are also powered by batteries, controlled wirelessly, and enclosed in aluminum boxes to resist the EMP noise from the discharge of the PGS machine. The size of the

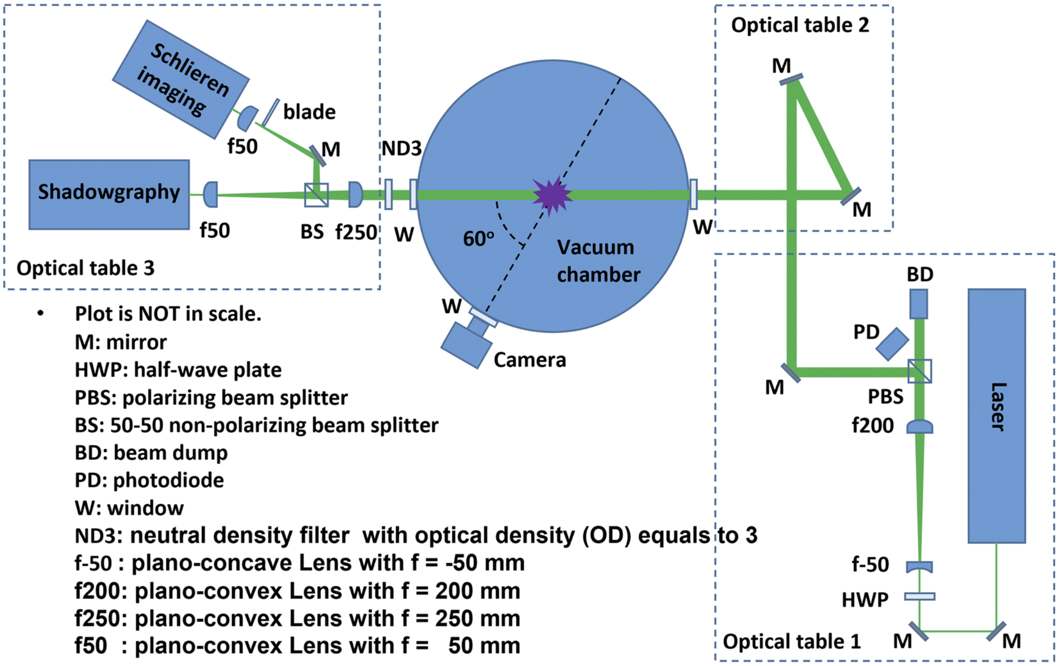

FIG. 6. The optical beam path of the laser diagnostics.

image sensors of the cameras is 7.9 mm in diagonal. Therefore, the expended beam is shrunk by five times using the lenses "f250" and "f50" so that the whole field of view fits into the image sensors.

The laser beam is split into two beams by a 50–50 non-polarizing beam-splitter cube (BS) on "Optical table 3" after passing through the region of interest. One is used for shadowgraph images,[23] and the other one is used for schlieren images.[23,24] Since the laser light passes through the beam-splitter cube (BS) after passing through the first lens of the beam shrinker, the two imaging systems share the same line of sight and the first lens ("f250") of the beam shrinker. A blade is used for the schlieren imaging system. The knife edge of the blade is in the vertical direction located at the focal point of the first lens of the beam shrinker. The blade blocks the entire focal spot so that only light deflected by lateral refractive index gradients reaches the camera. Thus, the schlieren image does not provide information on the magnitude of the density gradient. Nevertheless, the schlieren image helps us identify the boundary of the plasma generated by the PGS machine. Furthermore, temporal information can be obtained by taking images at different times. Note that only one image is taken in each shot. Therefore, multiple shots with laser triggered at different times are needed for studying the evolution of the generated plasma.

III. CALIBRATION OF THE DISCHARGE CURRENT

The PGS machine was tested by using four AWG16 wires with a length of 270 mm connected in parallel between two cylinders of the CTL as an inductive load. The system worked robustly without any prefires during the test. Figure 7 shows the traces from ten discharge currents overlapping accurately on top of each other. Except the high-frequency noise from the activation of the rail-gap switches occurred at the beginning of the discharge, the system ran in an underdamped RLC regime. Nevertheless, we are more interested in the first quarter period since our load, such as the conical-wire array introduced in Sec. IV A, is made of thin wires and burned out in the first quarter period. Equation (1) was used to fit the data for finding the characteristics of the discharge current,

$$I(t) = \mathrm{Unitstep}(t - t_0) I_0 \exp[-\gamma(t - t_0)] \sin[\omega(t - t_0)] + I_{\mathrm{off}}, \quad (1)$$

where I represents the current, I_0 is the amplitude of the current, γ is the damping rate, ω is the oscillating frequency, I_{off} is the offset of the signal, and t_o is the time that the current begins to increase. The fitted curve of one of the discharge currents is shown by the black dashed line in Fig. 7. The averaged quantities from ten shots are listed in Table I. A peak current of 135 ± 1 kA with a rise time, i.e., a quarter period, of 1592 ± 3 ns was generated. The corresponding inductance and resistance were calculated from ω and γ in Eq. (1). The calculated inductance was $L = \left[C \times \left(\omega^2 + \gamma^2\right)\right]^{-1} = 204 \pm 4$ nH, and the calculated resistance was $R = 2 \times \gamma \times L = 10.0 \pm 0.2$ mΩ. The variance was one standard deviation. The variance between ten shots was very small, which showed that the system was very robust and stable.

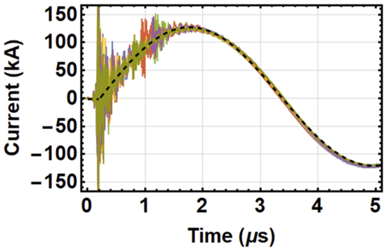

FIG. 7. Discharge current for the PGS machine: superposition of ten shots.

TABLE I. PGS machine parameters.

Capacitance	5 μF
V_{charge}	20 kV
Energy	1 kJ
I_{peak}	135 ± 1 kA
Rise time	1592 ± 3 ns
Inductance	204 ± 4 nH
Resistance	10.0 ± 0.2 mΩ

IV. IMPLOSIONS OF SMALL LOADS

We used the PGS machine to drive conical-wire arrays and x pinches for demonstrating the capability of studying high-energy-density plasmas that are relevant to the space environment, fusion, and spectroscopy.

A. Conical-wire arrays

The PGS machine was used to drive a conical-wire array as a demonstration of its capability for producing dynamic-plasma flows. This section will first briefly introduce the sequential events in an implosion of a conical-wire array. The geometry of the conical-wire array we used and how it was mounted on the system are also introduced. Finally, we show the temporal-integrated images from the self-emission of the plasma and ohmically heated wires in the visible light region and the time-resolved images using a Q-switch laser as the backlighter of the conical-wire array implosion.

1. Implosion process of the conical-wire array

A conical-wire array is a cylindrical array of discrete wires, where there exists a difference in the array diameters at the anode and cathode electrodes, Φ_{Anode} and Φ_{Cathode}, respectively, as illustrated in Fig. 8(a). The height and the inclination angle of the conical-wire array are h and θ, respectively.

The current delivered to the array heats the wires ohmically such that neutral cold wire cores are surrounded by lower-density, hot coronal plasma.[25,26] In time, the current amplitude (yellow arrows) becomes sufficient to accelerate the ionized plasma toward the axis, by a $\vec{J} \times \vec{B}$ force (red arrows), strongest at the cathode and less so at the anode. A steady plasma ablation from the wire cores occurs with an approximately constant ablation velocity $\vec{V}_{\mathrm{ab}}$ in the same direction as the $\vec{J} \times \vec{B}$ force.[27,28] Thus, the density of the plasma increases as mass from all wires accumulates on the axis. The radiation loss rate increases as the density increases,[29] and thus, a dense-cold precursor on the axis is eventually formed.

The time of the stagnation depends upon the strength of the $\vec{J} \times \vec{B}$ force. With a smaller diameter at the bottom of the conical-wire array than that at the top, the stagnation occurs earlier near

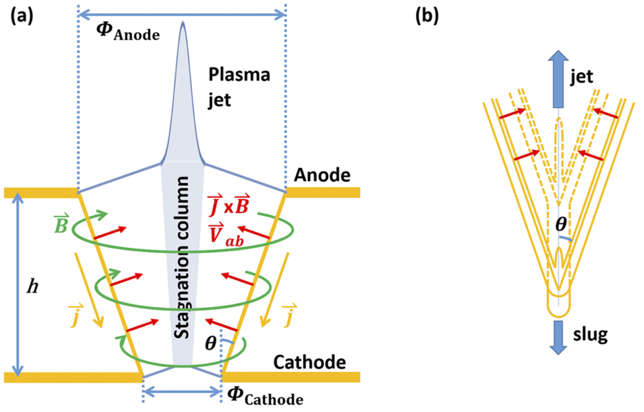

FIG. 8. (a) Conical-wire array. (b) Plasma jet and a slug produced in a Conical-wire array. Reprint with permission from Birkhoff *et al.*, J. Appl. Phys. **19**, 563 (1948). Copyright 1998 AIP Publishing.

the bottom than at the top. As a result, a zippered stagnation as the stagnation column occurs, as shown in Fig. 8(a).[28]

An up-going plasma jet is also formed during the stagnation process. Since the current has a radial component, the imploding velocity is slightly upward. Therefore, when the imploded material meets on the axis, it not only stagnates on the axis but also is redirected vertically, as shown in Fig. 8(b).[30,31] In the figure, solid lines are the imploded material in the earlier time, while dashed lines are at the later time. When the imploded materials collide, most of the material indicated as the slug moves downward with a lower speed. On the other hand, some of the materials are redirected upward with a much higher speed and form the up-going plasma jet. The typical wire materials are those with high atomic numbers, such as tungsten. Therefore, a significant radiative cooling occurs resulting in a jet that becomes highly collimated. Thus, a collimated plasma jet can be observed with appropriate diagnostics side-on.

2. Assembly of the conical-wire array

The conical-wire array we used consisted of four tungsten wires with an inclination angle of 30° with respect to the axis. The diameters of the wires were 20 μm. As shown in the inset of Fig. 9(a), the diameters at the bottom and the top of the conical-wire array were Φ_{Cathode} = 5 mm and Φ_{Anode} = 21 mm, respectively. The height of the conical-wire array h was 13.9 mm. To connect the conical-wire array to the outer cylinder of the CTL, four beams as the anode were used. There was a slot at the tip of each beam to ensure that each wire was connected to the center of the beam. On the other hand, a round disk as the cathode at the bottom of the conical-wire array was connected to the inner cylinder of the CTL. The cathode had a center hole with four slots uniformly distributed around the circumference. The slots also ensured that all wires connected to the cathode were at the required locations. To make the conical-wire array, each wire was first connected to the tip of each beam by a screw. Each wire would pass through the slot of each beam so that it was touching the center of the tip. An M2 screw as a weight was tightened to the free end of each wire. Each screw would pass through the center hole of the cathode and hang underneath the plate. Each wire would pass through one slot of the cathode so that the conical-wire array was formed. The weight of the screw would ensure that each wire was straight and touched the cathode and the anode firmly. Figure 9(b) shows a photograph of the actual conical-wire array before the shot.

The advantage of using four beams for connecting wires of the conical-wire array to the outer cylinder of the CTL is that a clear view from the side is provided between each beam. Everything all the way from the cathode to any locations within the field of view of the imaging system can be observed. Therefore, both the stagnation column and the plasma jet generated at the center of the conical-wire array can be observed simultaneously. Furthermore, the transition of plasma from the stagnation column to the plasma jet can be observed without being blocked by the holder of the conical-wire array. Moreover, the inclination angle can be adjusted by changing the length of beams. A twisted conical-wire array can also be built by rotating the beams if necessary. Nevertheless, only non-twisted conical-wire arrays were imploded in this work.

3. Implosion of the conical-wire array

In this section, experimental results of imploding conical-wire arrays are given. Time-integrated and time-resolved images are shown. Finally, the velocity of the plasma plume was calculated using the time-resolved schlieren images.

a. Time-integrated images. Figure 10 shows the side view of the implosion of the conical-wire array. First, four wires were heated ohmically by the current provided by the PGS machine. Therefore, self-emissions from wires are clearly observed in the image. Second, a little laser light was scattered by the beams that hold the wires and captured by the camera. Finally, the single plasma plume, including the stagnation column and the plasma jet, is observed. However, the fast radiative cooling may cause the length of the emitting part shorter than the actual length of the jet.[26,32] Therefore, the

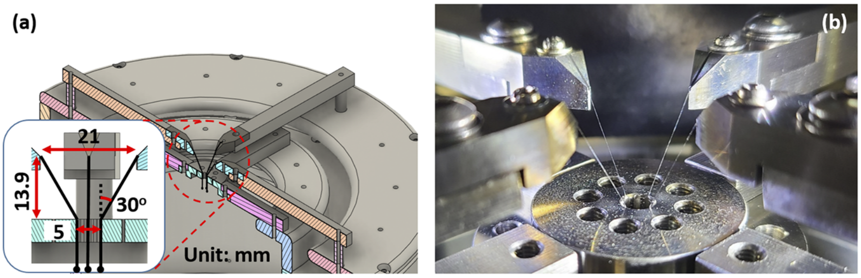

FIG. 9. (a) CAD drawing of the conical-wire array. (b) Photograph of the conical-wire array before implosion.

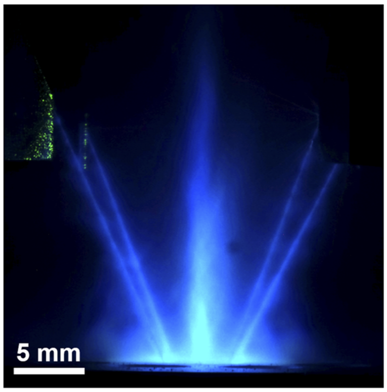

FIG. 10. Time-integrated, side-view image, enhanced by scaling the intensity range linearly from 0–64 to 0–255.

time-integrated image does not provide quantitative information about the plasma jet in detail. Nevertheless, it is used to confirm that the plasma jet was generated by the conical-wire array driven by the PGS machine in each shot.

b. Time-resolved images. Time-resolved shadowgraph images at different times are shown in Figs. 11(a)–11(d). Due to the internal delay of the triggering system for triggering the Q-switch laser, the earliest images were taken at 930 ± 20 ns after the PGS machine was activated. When currents flowed through the wires, they were ohmically heated and expanded over time. At the same time, plasma was ablated from the heated wires. The ablated plasma from the wires eventually merged at the center, thereby forming the plasma plume, including the stagnation column and the plasma jet as described in Sec. IV A 1. The zippering process is clearly observed from Figs. 11(a)–11(c). Turbulence structure in the plasma plume, which was smoothed out in time-integrated images, can also be observed. Therefore, it was difficult to determine the widths of the plasma plume at different heights. Nevertheless, the averaged width at different times can be obtained by analyzing the averaged intensity along the plasma plume and between two dashed lines in Figs. 11(a)–11(c). Figure 12(a) shows the averaged intensity across the plasma plume in Fig. 11(c) as an example. The profile was then fitted by a super-Gaussian function,

$$I(x) = a * \exp\left[-\left|\frac{x-b}{c}\right|^{d}\right] + e, \tag{2}$$

where a is the amplitude of the intensity, b is the center of the plasma plume, c is the width of the function, d is the power of the super-Gaussian function, and e is the background of the image. Note that the plasma plume in the shadowgraph was darker than the background. Therefore, a was a negative number. The power of the super-Gaussian function d was a fitted parameter since the profile varied between shot to shot and between different times. Then, we defined the full width at half maximum (FWHM) as the distance between the points where Eq. (2) equaled to $0.5a + e$, i.e., the distance between two red dots in Fig. 12(a). Two dashed lines in Fig. 12(a) present one standard deviation away from the fitted function. As a result, the width of the plasma plume was 0.09 ± 0.03 mm at 930 ns, 0.7 ± 0.3 mm at 975 ns, and 0.65 ± 0.07 mm at 985 ns. The plasma plume became wider as the plasma stagnated at the center.

Plasma plumes in shadowgraph images became blurred at the tip. It was not possible to determine the top edge of the plasma plume using shadowgraph images. Therefore, the time-resolved schlieren images, as shown in Figs. 11(e)–11(h), were used to determine the length of the plasma plume. All schlieren images were enhanced by linearly scaling the intensity range from 0–60 to 0–255. Nevertheless, raw data were used in data analysis. Ablations of the wire material and plasma plumes, including stagnation columns and plasma jets, are clearly shown in schlieren images even when the beam quality was not very good. However, since the vertical knife edge was used for taking schlieren images, the edge enhancement was not symmetrical. For example, although the ablated plasma from each wire is

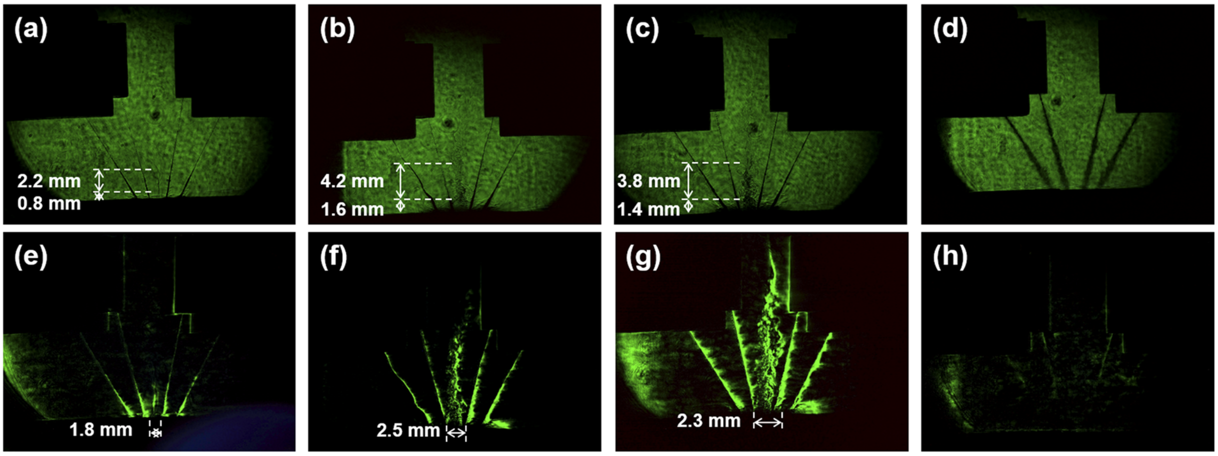

FIG. 11. (a)–(d) Shadowgraph images. (e)–(h) schlieren images. (a) and (e) were taken at $T = 930 \pm 20$ ns. (b) and (f) were taken at $T = 975 \pm 2$ ns. (c) and (g) were taken at $T = 985 \pm 3$ ns. (d) and (h) were taken at $T = 2945 \pm 2$ ns.

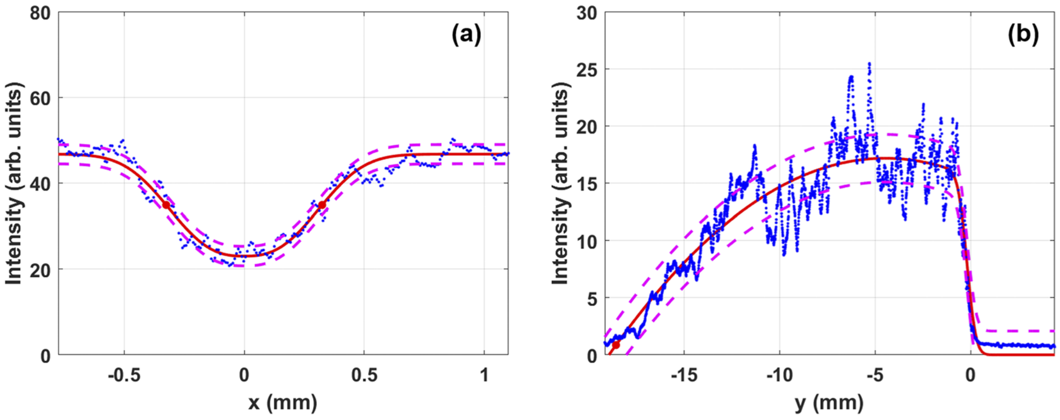

FIG. 12. (a) Intensity averaged across the plasma plume between two dashed lines from Fig. 11(c). (b) Averaged intensity along the plasma plume between two dashed lines from Fig. 11(g).

supposed to be nearly symmetrical around each wire, only ablations toward the right were shown in the schlieren images. Nevertheless, several features can still be observed. For example, wire modulation from the $m = 0$-type magnetohydrodynamics (MHD) instability of the wire ablation[33] is shown in the images. However, the seed of the instability was not well controlled, so the modulations were different between each wire and between each shot. Furthermore, the turbulence structure at the center is also shown. Most importantly, the length of the plasma plume in each image can be obtained. Figure 12(b) shows the averaged gray level between two vertical-dashed lines in Fig. 11(g) at different heights as an example. To obtain a smooth profile of the plasma plume, the profile was fitted by the following function:

$$I(y) = \left(a + by + cy^2\right) \times \frac{1}{2}\left[\mathrm{erf}\left(\frac{y-w}{d}\right) + 1\right], \tag{3}$$

where the quadratic equation was used to capture the rising edge at the top, while the error function was used to capture the fast following edge at the bottom. Then, the tip of the plasma plume was defined as the location of 5% of the maximum intensity indicated as the red dot in Fig. 12(b). Finally, we obtained the position of the tip of the plasma plume at different times, as shown in Fig. 13. The tip of the plasma plume moved very fast from 5 ± 1 mm at 930 ± 20 ns to 19 ± 1 mm at 1012 ± 1 ns, yielding an averaged velocity of 170 ± 70 km/s. In addition, if the plasma jet is defined as the plasma plume above the conical-wire array, which is 13.9 mm in height, the length of the plasma jet was $l_{\mathrm{jet}} \sim 5$ mm. The width of the plasma jet, on the other hand, was about $d_{\mathrm{jet}} \sim 2$ mm. It was the upper bound of the radial expansion of the plasma jet during the period that the jet propagated upward. Therefore, a rough estimation of the internal Mach number of the plasma jet was $M \sim V_{\mathrm{Z}}/V_{\mathrm{r}} \gtrsim l_{\mathrm{jet}}/(d_{\mathrm{jet}}/2) \sim 5$, where V_{Z} is the axial velocity of the plasma jet and V_{r} is the speed of the radial expansion of the plasma jet. Both the speed and the Mach number of the plasma jet are comparable to those of the solar wind.

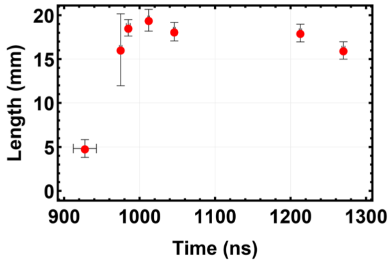

FIG. 13. Lengths of the plasma plumes at different times.

Furthermore, the speed of the ablated plasma $V_0 = 50 \pm 20$ km/s was then calculated using the following equation[30,31]:

$$V_{\mathrm{j}} = V_0 \frac{1 + \cos\theta}{\sin\theta}, \tag{4}$$

where V_{j} is the speed of the tip of the plasma plume and $\theta = 30^\circ$ is the inclination angle. The speed of the ablated plasma was much lower than that given in Ref. 28. It is reasonable since the power of our system was much less than those used in the reference.

After 985 ± 3 ns, the length of the plasma plume remained almost unchanged and faded out eventually while the wires kept expanding. Therefore, only one set of images at a later time [2945 ± 2 ns for Figs. 11(d) and 11(h)] are shown as an example. The wires kept expanding but did not move toward the axis of the conical-wire array, suggesting that current still flew through wires. It indicated that the remaining mass of wires was still significant so that only ablated plasma, not the whole wires, moved inward. It is the consequence of lower power provided by the PGS machine compared to those used in the reference. Therefore, wires with a smaller diameter are needed in the future.

B. X pinches

We used the PGS machine to drive an x pinch as the second example for demonstrating the capability of studying high-energy-density plasma. This section will first briefly introduce the sequential events in an implosion of the x pinch. The geometry of the x pinch we used and how it was mounted on the system are also introduced. Finally, we show the radiation from the cross point using temporal-integrated images.

1. Implosion process of the x pinch

An x pinch is formed by crossing two wires or multiple wires between the electrodes as shown in Fig. 14. When the pulsed-high current flows through the wires, they are first heated and ionized via Ohmic heating. The ionized gas (plasma) expends and forms a core-corona structure at the beginning when the magnetic pressure is too low to hinder the expansion.[34,35] At the cross point, a mini-diode is formed and starts being pinched by the magnetic field generated by the current. A hotspot with a radius less than 10 μm is subsequently formed due to the compression.[36] The temperature of the hotspot can reach a couple of keV at peak compression, generating an x-ray burst shorter than 1 ns in the range of k-shell emissions.[37] The mini-diode at the center eventually breaks and an electron beam is created between the gap. Broadband hard x ray up to 200 keV with larger emitting size (~100 μm)[38] can be generated by the electron beam. Depending on the applications, wires can be made of materials with a higher atomic number, such as tungsten, or a lower atomic number, such as carbon, if harder or softer x-ray line emission is needed, respectively.

Traditionally, an x pinch is driven by a pulse current with a rise time (a quarter of period) in the order of 100 ns with a current rising speed $dI/dt > 1$ kA/ns.[39,40] Nevertheless, several studies have shown that x pinches driven by a slow current pulse ($dI/dt \leq 0.3$ kA/ns) with a rise time of microseconds can still generate soft x rays ($\leq$8 keV).[41,42] In the PGS machine, the current rising speed $dI/dt|_{\max} \sim 0.13$ kA/ns. It may be too slow to generate soft x rays via driving an x pinch. However, it can be used to study the cross-point dynamics and the coronal plasma. Therefore, we used the PGS machine to drive the x pinch.

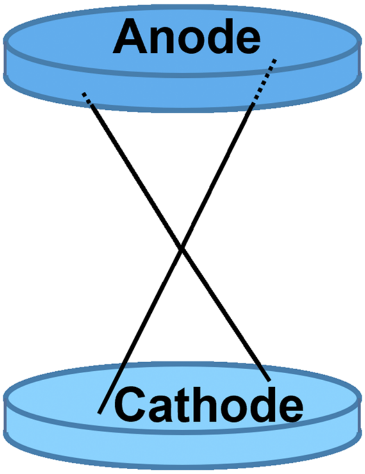

FIG. 14. The setup of x pinches. Two wires or multiple wires crossing each other form a cross point between the anode and the cathode.

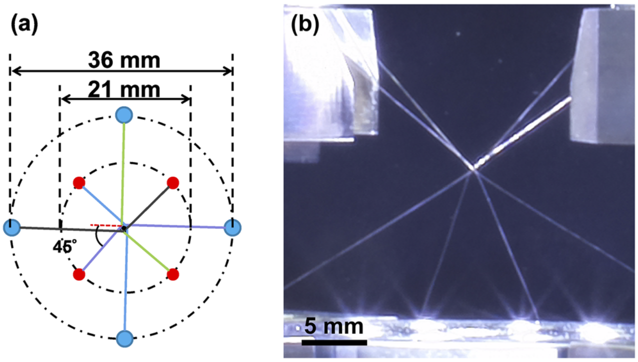

FIG. 15. (a) How the wires were bent in the x pinch. (b) The photograph of the x pinch before being imploded.

2. Assembly of the x pinch

Figure 15(a) shows the schematic of how the x pinch was built. We used the same beams and the same round disk that were used for holding the conical-wire array. Four tungsten wires with diameters of 20 μm were also used. The difference was how the wires were held between the beams and the round disk. As shown in Fig. 15(a), four wires were bent 45° after crossing each other forming a cross point. Diameters at the anode and cathode electrodes are 36 and 21 mm, respectively. Finally, the wires were fixed to the round disk similar to the way in conical-wire arrays. Figure 15(b) shows the x pinch before the experiment. Four wires were touching each other firmly at the cross point.

3. Implosion of the x pinch

Figure 16(a) shows the time-integrated side-view image of the implosion of the x pinch in visible light. Similar to the implosion of the conical-wire array, four wires were heated ohmically by the current provided by the PGS machine. Therefore, self-emissions from the wires are clearly observed in the image. Furthermore, two plasma plumes, one went up and one went down, are observed. They are expected since the upper half and the bottom half of the x pinch are basically two conical-wire arrays in opposite directions. In addition,

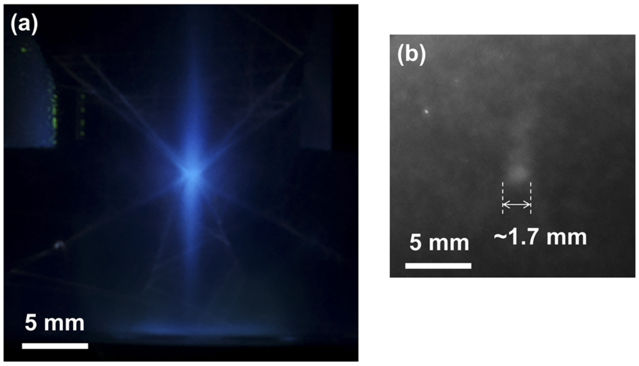

FIG. 16. The time-integrated image of the x pinch from the side in the range of visible light (a) and with a wavelength less than 150 nm (b).

the cross point was the brightest point as expected. Moreover, we used a pinhole camera to take the time-integrated side-view image of the implosion. The magnification factor of the camera was 1. The diameter of the pinhole was 50 μm. The camera was capable of recording photons with a wavelength less than 150 nm, i.e., photo energy of more than 8 eV. The image taken by the pinhole camera is shown in Fig. 16(b). A bright spot with a diameter of ~1.7 mm corresponded to the radiation from the cross point. Although the radiation from the cross point was much weaker in intensity and much bigger in size compared to those from a traditional x pinch, the PGS machine can be used to study the cross-point dynamics and the coronal plasma under a slow current pulse in the future.

V. SUMMARY

A compact pulsed-power system has been developed, suitable for the study of plasmas covering a wide range of parameter space. The system design is based on the use of a low impedance, parallel-plate transmission line that conducts discharge current from the capacitor banks to a target placed in the vacuum chamber. The stored energy is 1 kJ when the system is charged to 20 kV.

The system performance has been calibrated, and several diagnostics installed quantify the implosion and stagnation of an active-plasma load produced by an imploded conical-wire array. The length of the plasma plume reached 19 ± 1 mm at 1012 ± 1 ns after the system was activated. Various features were observed, such as $m = 0$-type MHD instability, wire ablations, and turbulence in the plasma plume. The speed of ablated plasma from the tungsten wires is estimated as $V_0 = 50 \pm 20$ km/s. The speed of the plasma jet measured from the schlieren images was 170 ± 70 km/s with a Mach number of $\gtrsim 5$. These speeds are comparable to that observed for the solar wind. Future studies are expected to continue to use the PGS machine to generate and study plasma flows typical of the space environment.

ACKNOWLEDGMENTS

The authors are grateful to Neoway Chemicals Co., Ltd., for providing high-density foam. This work was supported by the Ministry of Science and Technology (MOST), Taiwan, under Award Nos. 105-2112-M-006-014-MY3 and 109-2112-M-006-011.

AUTHOR DECLARATIONS

Conflict of Interest

The authors have no conflicts to disclose.

DATA AVAILABILITY

The data that support the findings of this study are available from the corresponding author upon reasonable request.

REFERENCES

[1] D. Smith, P. Ingwersen, L. Bennett, J. Boyes, D. Anderson, J. Greenly, R. Sudan, and D. Hammer, in *Digest of Technical Papers. Tenth IEEE International Pulsed Power Conference* (IEEE, 1995), p. 1449.

[2] J. B. Greenly, J. D. Douglas, D. A. Hammer, B. R. Kusse, S. C. Glidden, and H. D. Sanders, Rev. Sci. Instrum. **79**, 073501 (2008).

[3] I. H. Mitchell, J. M. Bayley, J. P. Chittenden, J. F. Worley, A. E. Dangor, M. G. Haines, and P. Choi, Rev. Sci. Instrum. **67**, 1533 (1996).

[4] B. S. Bauer, V. L. Kantsyrev, F. Winterberg, A. S. Shlyaptseva, R. C. Mancini, H. Li, and A. Oxner, in *The 4th International Conference on Dense Z-Pinches* (ASCE, 1997), Vol. 409, p. 153.

[5] D. V. Rose, D. R. Welch, E. A. Madrid, C. L. Miller, R. E. Clark, W. A. Stygar, M. E. Savage, G. A. Rochau, J. E. Bailey, T. J. Nash *et al.*, Phys. Rev. Spec. Top.–Accel. Beams **13**, 010402 (2010).

[6] M. E. Savage, K. LeChien, M. Lopez, B. Stoltzfus, W. Stygar, D. Artery, J. Lott, and P. Corcoran, in *2011 IEEE Pulsed Power Conference* (IEEE, 2011).

[7] B. M. Koval'chuk, V. A. Vizir', A. A. Kim, E. V. Kumpyak, S. V. Loginov, A. N. Bastrikov, V. V. Chervyakov, N. V. Tsoi, P. Monjaux, and D. Kh'yui, Russ. Phys. J. **40**, 1142 (1997).

[8] M. G. Mazarakis, W. E. Fowler, A. A. Kim, V. A. Sinebryukhov, S. T. Rogowski, R. A. Sharpe, D. H. McDaniel, C. L. Olson, J. L. Porter, K. W. Struve *et al.*, Phys. Rev. Spec. Top.–Accel. Beams **12**, 050401 (2009).

[9] A. A. Kim, M. G. Mazarakis, V. A. Sinebryukhov, B. M. Kovalchuk, V. A. Visir, S. N. Volkov, F. Bayol, A. N. Bastrikov, V. G. Durakov, S. V. Frolov *et al.*, Phys. Rev. Spec. Top.–Accel. Beams **12**, 050402 (2009).

[10] A. A. Kim and M. G. Mazarakis, IEEE Trans. Plasma Sci. **48**, 749 (2020).

[11] R. M. Gilgenbach, M. R. Gomez, J. C. Zier, W. W. Tang, D. M. French, Y. Y. Lau, M. G. Mazarakis, M. E. Cuneo, M. D. Johnston, B. V. Oliver *et al.*, AIP Conf. Proc. **1088** 259 (2009).

[12] F. Conti, J. Valenzuela, V. Fadeev, N. Aybar, D. Reisman, A. Williams, G. Collins, J. Narkis, M. Ross, F. Beg *et al.*, Phys. Rev. Accel. Beams **23**, 090401 (2020).

[13] P.-A. Gourdain, M. Evans, B. Foy, D. Mager, R. McBride, and R. Spielman, "Hades: A high amperage driver for extreme states," arXiv:1705.04411.

[14] A. D. Van Drie, "Thermonuclear fusion in a staged Z-pinch," Ph.D. thesis, University of California, Irvine, 2001.

[15] G. R. Neil and R. S. Post, Rev. Sci. Instrum. **49**, 401 (1978).

[16] E. Lopez, G. Bennett, R. Bartsch, J. Cochrane, J. Griego, R. Hicks, W. Hinckley, K. Hosack, R. Kasik, A. Marquez *et al.*, in *Digest of Technical Papers. 11th IEEE International Pulsed Power Conference (Cat. No.97CH36127)* (IEEE, 1997).

[17] C. Grabowski, J. H. Degnan, T. Cavazos, D. G. Gale, C. Gilman, W. Sommars, T. P. Intrator, J. M. Taccetti, B. Waganaar, R. E. Siemon, and G. A. Wurden, IEEE Trans. Plasma Sci. **30**, 1905 (2002).

[18] Z. H. Sholapurwala, in *National Power Systems Conference* (IEEE, 2004), p. 1142.

[19] C. Grabowski, J. H. Degnan, J. V. Parker, J. F. Camacho, S. K. Coffey, R. K. Delaney, M. T. Domonkos, T. P. Intrator, A. G. Lynn, J. McCullough *et al.*, IEEE Trans. Plasma Sci. **44**, 1997 (2016).

[20] P.-Y. Chang, C.-J. Hsieh, M.-F. Huang, M.-C. Jheng, Y.-C. Lin, J.-K. Liu, and S.-H. Yang, Rev. Sci. Instrum. **91**, 114703 (2020).

[21] See https://quantel-laser.com/home.html for Lumibird.

[22] See https://thorlabs.com/ for Thorlabs, Inc.

[23] G. C. Burdiak, *Cylindrical Liner Z-Pinches as Drivers for Converging Strong Shock Experiments* (Springer International Publishing, 2016).

[24] G. S. Settles, *Schlieren and Shadowgraph Techniques* (Springer, Berlin, Heidelberg, 2006).

[25] D. H. Kalantar and D. A. Hammer, Phys. Rev. Lett. **71**, 3806 (1993).

[26] S. V. Lebedev, J. P. Chittenden, F. N. Beg, S. N. Bland, A. Ciardi, D. Ampleford, S. Hughes, M. G. Haines, A. Frank, E. G. Blackman *et al.*, Astrophys. J. **564**, 113 (2002).

[27] S. V. Lebedev, F. N. Beg, S. N. Bland, J. P. Chittenden, A. E. Dangor, M. G. Haines, K. H. Kwek, S. A. Pikuz, and T. A. Shelkovenko, Phys. Plasmas **8**, 3734 (2001).

[28] D. J. Ampleford, S. V. Lebedev, S. N. Bland, S. C. Bott, J. P. Chittenden, C. A. Jennings, V. L. Kantsyrev, A. S. Safronova, V. V. Ivanov, D. A. Fedin *et al.*, Phys. Plasmas **14**, 102704 (2007).

[29] S. C. Bott, S. V. Lebedev, D. J. Ampleford, S. N. Bland, J. P. Chittenden, A. Ciardi, M. G. Haines, C. Jennings, M. Sherlock, G. Hall *et al.*, Phys. Rev. E **74**, 046403 (2006).

[30] G. Birkhoff, D. P. MacDougall, E. M. Pugh, and S. G. Taylor, J. Appl. Phys. **19**, 563 (1948).

[31] F. Winterberg, J. Fusion Energy **30**, 283 (2010).

[32] S. V. Lebedev, D. Ampleford, A. Ciardi, S. N. Bland, J. P. Chittenden, M. G. Haines, A. Frank, E. G. Blackman, and A. Cunningham, Astrophys. J. **616**, 988 (2004).

[33] C. J. Garasi, D. E. Bliss, T. A. Mehlhorn, B. V. Oliver, A. C. Robinson, and G. S. Sarkisov, Phys. Plasmas **11**, 2729 (2004).

[34] G. S. Sarkisov, P. V. Sasorov, K. W. Struve, and D. H. McDaniel, J. Appl. Phys. **96**, 1674 (2004).

[35] V. I. Oreshkin, S. A. Chaikovsky, A. P. Artyomov, N. A. Labetskaya, A. V. Fedunin, A. G. Rousskikh, and A. S. Zhigalin, Phys. Plasmas **21**, 102711 (2014).

[36] T. A. Shelkovenko, S. A. Pikuz, J. D. Douglass, R. D. Mcbride, J. B. Greenly, and D. A. Hammer, IEEE Trans. Plasma Sci. **34**, 2336 (2006).

[37] T. A. Shelkovenko, D. B. Sinars, S. A. Pikuz, K. M. Chandler, and D. A. Hammer, Rev. Sci. Instrum. **72**, 667 (2001).

[38] T. Shelkovenko, S. Pikuz, and D. Hammer, J. Biomed. Sci. Eng. **08**, 747 (2015).

[39] R. K. Appartaim and B. T. Maakuu, Phys. Plasmas **15**, 072703 (2008).

[40] G. S. Jaar and R. K. Appartaim, J. Appl. Phys. **123**, 213301 (2018).

[41] R. K. Appartaim, J. Appl. Phys. **114**, 083304 (2013).

[42] G. W. Collins, M. P. Valdivia, T. Zick, R. E. Madden, M. G. Haines, and F. N. Beg, Phys. Plasmas **20**, 042704 (2013).